Journal of Solid State Chemistry 184 (2011) 1054–1062

Contents lists available at ScienceDirect

Journal of Solid State Chemistry

journal homepage: www.elsevier.com/locate/jssc

Synthesis, characterization and photocatalytic properties of novel zinc germanate nano-materials

Venkata Bharat Ram Boppana, Nathan D. Hould, Raul F. Lobo *

Center for Catalytic Science and Technology, Department of Chemical Engineering, University of Delaware, Newark, DE 19716, USA

ARTICLE INFO

Article history:
Received 7 December 2010
Received in revised form
16 February 2011
Accepted 20 February 2011
Available online 9 March 2011

Keywords:
Photocatalysis
Photocatalyst
Zn_2GeO_4
Morphology
Hydrothermal
Methylene blue

ABSTRACT

We report the first instance of a hydrothermal synthesis of zinc germanate (Zn_2GeO_4) nano-materials having a variety of morphologies and photochemical properties in surfactant, template and catalyst-free conditions. A systematic variation of synthesis conditions and detailed characterization using X-ray diffraction, ultraviolet–visible diffuse reflectance spectroscopy, Raman spectroscopy, electron microscopy, X-ray photoelectron spectroscopy and small angle X-ray scattering led to a better understanding of the growth of these particles from solution. At 140 °C, the zinc germanate particle morphology changes with pH from flower-shaped at pH 6.0, to poly-disperse nano-rods at pH 10 when the Zn to Ge ratio in the synthesis solution is 2. When the Zn to Ge ratio is reduced to 1.25, mono-disperse nano-rods could be prepared at pH 7.5. Nanorod formation is also independent of the addition of cetyltrimethylammonium bromide (CTAB), in contrast to previous reports. Photocatalytic tests show that Zn_2GeO_4 nano-rods (by weight) and flower shaped (by surface area) are the most active for methylene blue dye degradation among the synthesized zinc germanate materials.

1. Introduction

Photocatalysis is the process of choice for degradation of diluted organic compounds and a potentially important technology for hydrogen production from water. Photocatalysts composed of d^0 elements have been the focus of many studies (e.g. TiO_2) [1,2], but more recently the emphasis has shifted to photocatalysts composed of d^{10} elements since they are also predicted to be photocatalytically active by quantum chemistry [3]. These investigations have led to several new d^{10} mixed-metal oxides and oxynitrides [3–5] active for a variety of photocatalytic applications [3,6,7].

Zinc germanate is an example of a photocatalyst comprised of d^{10} cations (i.e., Zn^{2+} and Ge^{4+}). It is composed of GeO_4 and ZnO_4 tetrahedra (Zn is in two different crystallographic positions) bridged by oxygen atoms in a hexagonal unit cell ($a=b\approx 14.23$ Å and $c\approx 9.53$ Å) [8]. Most preparations of zinc germanate have been completed in non-hydrothermal conditions such as thermal evaporation [9], magnetron sputtering [10] and high temperature solid–solid reactions [11]. The drawback of these processes is that high temperatures are required, resulting in products with low surface areas and high concentration of defects. Wet chemistry synthesis of photocatalysts is an attractive low temperature alternative that has been studied before: photocatalysts typically show variations in particle shape and size dependent on the hydrothermal synthesis conditions [12–15]. A few studies of sol–gel synthesis of d^{10} mixed-oxide photocatalysts have been reported [16,17]. For example Jianhui et al. [16] have synthesized photocatalytically active Zn_2GeO_4 nano-rods hydrothermally in the presence of CTAB surfactant but few other novel particle morphologies have been grown so far.

Here we describe the formation of Zn_2GeO_4 with novel morphologies in surfactant-free solution conditions. Photocatalytic activity depends on a variety of factors like surface area, crystallinity, morphology and defects, factors that can be controlled in the hydrothermal synthesis step. Synthesis parameters such as pH (6, 7.5, 10), precursor Zn/Ge ratio (2, 1.25), synthesis temperature (room temperature i.e. 25, 140 °C), synthesis time (2, 8, 16, 24 h) and surfactant (CTAB) were modified systematically. The structure and properties of Zn_2GeO_4 synthesized under these different conditions are characterized by X-ray diffraction (XRD), N_2 adsorption isotherms, ultraviolet–visible diffuse reflectance spectroscopy (UV–vis), Raman spectroscopy, scanning electron microscopy (SEM), X-ray photoelectron spectroscopy (XPS), thermogravimetric analysis (TGA) and small angle X-ray scattering (SAXS). The photocatalytic activities of the products are also tested using methylene blue degradation as a model reaction showing that the nano-rods (by weight) and the flower-shaped (by surface area) particles are the most active. The novel zinc germanate particles reported here could prove useful for photocatalytic water splitting [11,18],

* Corresponding author. Fax: +1 302 831 1048.
E-mail address: lobo@udel.edu (R.F. Lobo).

0022-4596/$ - see front matter © 2011 Elsevier Inc. All rights reserved.
doi:10.1016/j.jssc.2011.02.022

oxidation [16,19], even CO_2 reduction [20] and other opto-electronic applications.

2. Experimental

2.1. Synthesis

Zinc germanate samples were synthesized from GeO_2 (trigonal, 99.99%, Strem Chemicals) and zinc nitrate hexahydrate (98%, Strem Chemicals). The Zn to Ge atomic ratio (from the precursor) used was either 2 (stoichiometric) or 1.25 (excess Ge). 2.006 or 1.255 g of $Zn(NO_3)_2 \cdot 6H_2O$ for the stoichiometric Ge and excess Ge synthesis conditions, respectively, was initially added to 80 ml deionized water and stirred for 15 min. To this solution 0.3527 g of GeO_2 was added and stirred for an hour. Under continuous stirring, aqueous ammonia solution (27%, Fisher) was then added dropwise until the pH of the solution reached 6, 7.5 or 10. After stirring for 30 min at room temperature (25 °C) the solution was transferred to 120 ml Teflon-lined Parr autoclaves and held at 140 °C under static conditions for 2, 8, 16 or 24 h. The autoclave was then quenched in cold water. The products prepared at 25 °C were continuously stirred in a closed PPE vessel. The pH and conductivity were measured at various points before, during (for 25 °C samples) and after the reaction. The resulting precipitate was separated from the supernatant by centrifugation at 4400 rpm and washed multiple times with DI water. The product was then dried at 80 °C overnight prior to characterization and photocatalytic testing. In some synthesis, 0.1 g cetyltrimethylammonium bromide (CTAB) was added before the addition of aqueous ammonia and stirred for 30 min to study the effect of surfactant on particle morphology and activity.

The synthesis conditions for all the samples are listed in Table 1. The nomenclature used in this report is as follows; all samples with *stoichiometric* Ge (at 25 °C) have sample names that start with Si and those obtained at 140 °C are named as STi. Similarly, zinc germanate products synthesized in solutions with *excess* Ge are named Ei if obtained at 25 °C and as ETi if the temperature was maintained at 140 °C. i indicates the pH employed in all cases, $i=1$, 2 and 3 indicates the pH at 6, 7.5 and 10, respectively. Other parameters such as time and presence of CTAB are indicated after the sample name. For example, ET2_16_C indicates the sample synthesized at pH 7.5 and 140 °C for 16 h with CTAB.

2.2. Analytical

2.2.1. Characterization

Powder X-ray diffraction (XRD) data were collected on a Philips X′pert diffractometer using a Cu$K\alpha$ source. The patterns were obtained from 5° to 70° $2-\theta$ using a step size of 0.02° $2-\theta$ and 2.5 s per step. UV–vis spectra were obtained on a Jasco V-550 spectrometer equipped with an ISV-469 integrating sphere from 850 to 220 nm with a bandwidth of 1 nm and using MgO as a reference material. Adsorption isotherms were collected on a Micromeritics ASAP 2010 using N_2 as the adsorbate at 77 K and the Brunauer, Emmett and Teller (BET) surface areas calculated with P/P_0 values between 0.05 and 0.3. Scanning electron microscope (SEM) images were obtained on a JEOL JSM7400F microscope with a field emission gun capable of 1.5 nm resolution. The imaging using the SEM and elemental analysis using energy dispersive analysis (EDAX) were done at a voltage of 3 and 20 kV, respectively, and emission current 10 μA. Raman spectra were measured using a 100 mW Neon laser at a wavelength of 785 nm. Spectra were collected for the range of 80–1530 cm^{-1} using 3–5 cm^{-1} step size, 20× objective, 50 × 1000 μm^2 aperture and integration time of 60 s with 3 co-additions. The background was calibrated every 1000 s. The cosmic spike and florescence corrections were not utilized. X-ray photoelectron spectroscopy (XPS) measurements were taken with an Al standard source with the neutralizer switched on at 100 eV energy and 25 mA current. The survey scan parameters are 1.6 eV $step^{-1}$, 100 ms $step^{-1}$ and pass energy of 187.85 eV in 20 min. The multi-scans were done for Ge $2p_{3/2}$, Zn $2p_{3/2}$, O 1s and C 1s with the following conditions; 0.125 eV $step^{-1}$, 50 ms $step^{-1}$, 58.7 eV pass energy and 3 sweeps in 75 min. Sample charging was reduced using a neutralizer gun running at 25 mA and 100 eV, though this did not remove all the peak asymmetry at low energies. Thermogravimetric analyses (TGA) were conducted on a Mettler Toledo TGA/DSC 1 STARe system from 25 to 500 °C at 3 °C min^{-1} and 50 ml min^{-1} of air flow.

The general power law derived by Davis and Mott [21] was used to determine the band gap energies. The equation is

$$\alpha\hbar\omega \propto (\hbar\omega - E_g)^n$$

Table 1
The reaction conditions, solution properties and product properties for the materials prepared in this report. The synthesis time is 8 h, the temperature is 25 or 140 °C and pH and initial Zn/Ge ratios are changed as indicated. The sample ID in column 1 is used throughout the manuscript for identification of the samples.

Sample	Temperature (°C)	Yield (g)	Yield based on Zn (%)	Nominal pH	Measured initial pH	Final pH	Specific surface area of product (m^2/g)	Band gap of product (eV)
S1_8	25	0.16	–	6	5.98	5.13	–	–
S2_8	25	0.84	93	7.5	7.49	7.55	62	4.61
S3_8	25	0.61	–	10	9.99	9.90	35	4.58
ST1_8	140	0.21	23	6	5.95	5.16	5	4.63
ST2_8[a]	140	0.81	90	7.5	7.73	8.07	57	4.68
ST3_8[a]	140	0.77	85	10	10.0	10.1	43	4.65
ST2_8_C	140	0.79	88	7.5	7.69	8.05	42	4.70
E1_8	25	0.09	–	6	5.95	5.15	–	–
E2_8	25	0.53	–	7.5	7.57	7.79	65	4.58
E3_8	25	0.33	–	10	10.00	9.92	35	4.69
ET1_8	140	0.19	34	6	6.2	5.38	4	4.65
ET2_8[a]	140	0.41	73	7.5	7.66	8.11	40	4.70
ET3_8[a]	140	0.34	60	10	10.01	9.98	60	4.68
ET2_8_C	140	0.43	–	7.5	7.69	8.12	28	4.66

[a] These are samples further tested for variations with respect to the synthesis time to optimize the photocatalytic activity (2, 8, 16 and 24 h). The maximum yields are 0.9 and 0.56 g for the stoichiometric and excess Ge synthesis conditions. The yield percentages for the materials synthesized at 25 °C are not provided as pure phase zinc germanate is not obtained (except S2_8, see Fig. 1 and Supporting Information). The ET_8_C product contains CTAB as determined by TGA measurements (Fig. S8).

where, α is the absorption coefficient in Kubelka–Munk $F(R_\infty)$ units, $\hbar\omega = h\nu$ is the photon energy, E_g is the band gap of the material and n is a constant equal to 0.5, 1.5, 2 and 3 for direct allowed, direct forbidden, indirect allowed and indirect forbidden, respectively. For the band gap calculations direct allowed transitions ($n=0.5$) are assumed since Zn_2GeO_4 [16] is a direct band gap semiconductor. In practice, the raw data is plotted with $[F(R_\infty)\,h\nu]^2$ as the y-axis and photon energy ($h\nu$) as the y-axis. The band gap is then determined from a straight line fit for the linear region of the graph.

2.2.2. Liquid analysis

The conductivity of solutions was measured with a VWR scientific model 2052 EC meter. The hydronium ion concentrations (pH) were determined using a Corning 355pH/ion analyzer equipped with an Orion Ross electrode (model 8104). Before collecting pH data the meter was calibrated using pH 4, 7, 10 and 12 standard buffer solutions. SAXS patterns of the solutions at the end of the synthesis time were collected on a SAXSess instrument (Anton-Paar) using line collimated Cu$K\alpha$ radiation (1.542 Å) and a phosphor image plate. The sample holder is a TCS120 (Anton-Paar) fitted for liquid samples using a quartz capillary (1 mm diameter). The q-scale is determined relative to the maximum intensity of the primary attenuated beam ($q=0$) which subsequently was used to scale the intensity of the scattering pattern ($I(q=0)=1$). Afterwards a water background is subtracted from the scattering pattern.

2.2.3. Photocatalytic experiments

These were conducted using methylene blue as a model compound. Initially the photocatalyst (1 g l^{-1}) was added to 100 ml of 5 mg l^{-1} methylene blue solution. The solution was stirred in the dark for 90 min to achieve adsorption–desorption equilibrium as determined by consecutive and identical UV–vis spectral readings. The photo-reactor light source was then turned on. The light source is a 450 W Oriel xenon lamp with a 1.5″ beam turner connected to an Oriel lamp power supply. A water filter was inserted in between the lamp source and the methylene blue solution to remove IR radiation. Approximately 3 ml of the methylene blue solution was pipetted out at regular intervals and centrifuged at 3220 rcf for 20 min to remove any solid particles. The percentage of degradation of the dye was then evaluated using a Jasco V-550 UV–vis spectrometer. Methylene blue is known to degrade via a Langmuir–Hinshelwood model which is represented by [22,23]

$$r = -\frac{dc}{dt} = k'\frac{K_{LH}C}{1+K_{LH}C} \tag{1}$$

where r is the rate of degradation of methylene blue (mg l^{-1} min^{-1}), k' is the reaction rate constant (1 min^{-1}), K_{LH} is the Langmuir–Hishelwood dye adsorption constant and C is the concentration (mg/l). As for these dye degradation experiments, the concentration of the dye is generally in ppm levels (in our case 5 mg/l) the denominator can be simplified to; $1+K_{LH}C \approx 1$. The equation then becomes a simple first order rate expression and the concentration at any time can be expressed as

$$-\frac{dc}{dt} = k'K_{LH}C = kC \tag{2}$$

$$C = C_0 e^{-kt} \tag{3}$$

where C_0 is the initial concentration (mg l^{-1}). Some of the important parameters of the first order reaction are

$$r_0 = C_0 k \tag{4}$$

$$t_{1/2} = \frac{\ln(2)}{k} \tag{5}$$

where, r_0 is the initial rate of the equation i.e., $-dc/dt|_{t=0}$ and $t_{1/2}$ is the time required to degrade 50% of the initial methylene blue reactant. Control experiments were conducted with no catalyst in UV light for which only 2% photolytic degradation was obtained in 2 h. The dark adsorption with ET2_8 nano-rods is only 4%.

3. Results and discussion

3.1. Hydrothermal synthesis of Zn_2GeO_4

The synthesis of zinc germanate was investigated at different synthesis compositions and temperatures. At 140 °C, pure zinc germanate was obtained for all the synthesis compositions studied (Fig. 1B and D). Yields are 73–90% based on zinc at pH 7.5, and 60–85% at pH 10 (see Table 1). In all the samples synthesized at high temperature, a decreasing crystallite size with increasing pH was observed. At 25 °C mixed phase products are usually obtained. Further experiments revealed that all the samples synthesized at 25 °C show low photocatalytic activities for the degradation of methylene blue or the degradation is via N-demethylation; therefore the report centers on Zn_2GeO_4 samples synthesized at 140 °C. The low photocatalytic activities for the samples synthesized at 25 °C are because these are not pure phase zinc germanate particles and also have low crystallinity (Fig. 1). Both features tend to reduce photocatalytic activity. Further characterization details on the samples synthesized at 25 °C are summarized in Supporting Information.

SEM micrographs indicate that the zinc germanate morphology is highly dependent on the synthesis pH; mono-disperse nano-rods are only obtained when the pH is only 7.5 and with excess Ge in the synthesis gel (ET2_8, Fig. 2D). Using stoichiometric Ge and a pH of 10, the product is poly-morphic, showing the presence of poly-disperse nano-rods and globular particles (ST3_8, Fig. 2E). The products with nano-rod morphologies have a larger crystallite size (as determined by the FWHM of the 006 peak) as compared to the other morphologies (Table 2) and also indicating preferential growth along the c-direction [24]. Interestingly, Zn_2GeO_4 prepared at pH of 6.0 (ST1_8 and ET1_8) has a flower-like morphology independent of the germanium content in the initial solution (Fig. 2A and B). When using excess Ge in the synthesis gel, there is a transformation in the morphology of Zn_2GeO_4 from flower-shaped at pH 6.0 to mono-disperse nano-rods at pH 7.5 and finally to globular particles at pH 10.0. Davis et al. [25] have observed similar interesting morphological changes of GeO_2 with increasing initial germania concentration. The addition of surfactant (CTAB) was investigated at a number of conditions and was found to have no effect on particle morphology (see Fig. S2 in the SI), in contrast to previous studies [16]. The SAXS patterns of the final synthesis solutions with or without CTAB are essentially identical (Fig. 3) implying that the addition of surfactant does not influence the particle growth and morphology. The reason for the different results between different laboratories is not understood at this time.

3.2. Composition and local structure

All the samples synthesized at 140 °C have the stoichiometric Zn/Ge ratio of 2 as determined from EDAX. Even when there is excess Ge in the synthesis solution the product obtained is stoichiometric Zn_2GeO_4. In contrast, when excess Zn was introduced to the reaction solution the product was always a physical mixture of ZnO and Zn_2GeO_4 (see Fig. S3 in the SI).

The surface composition of the zinc germanate products was investigated using XPS and from these data it is clear that all the samples synthesized are made of Ge^{4+} and Zn^{2+} and there is no evidence of any reduced forms of the metals. For Zn_2GeO_4 samples, the electronic binding energy (EBE) is shifted positively by ≈ 0.7 eV

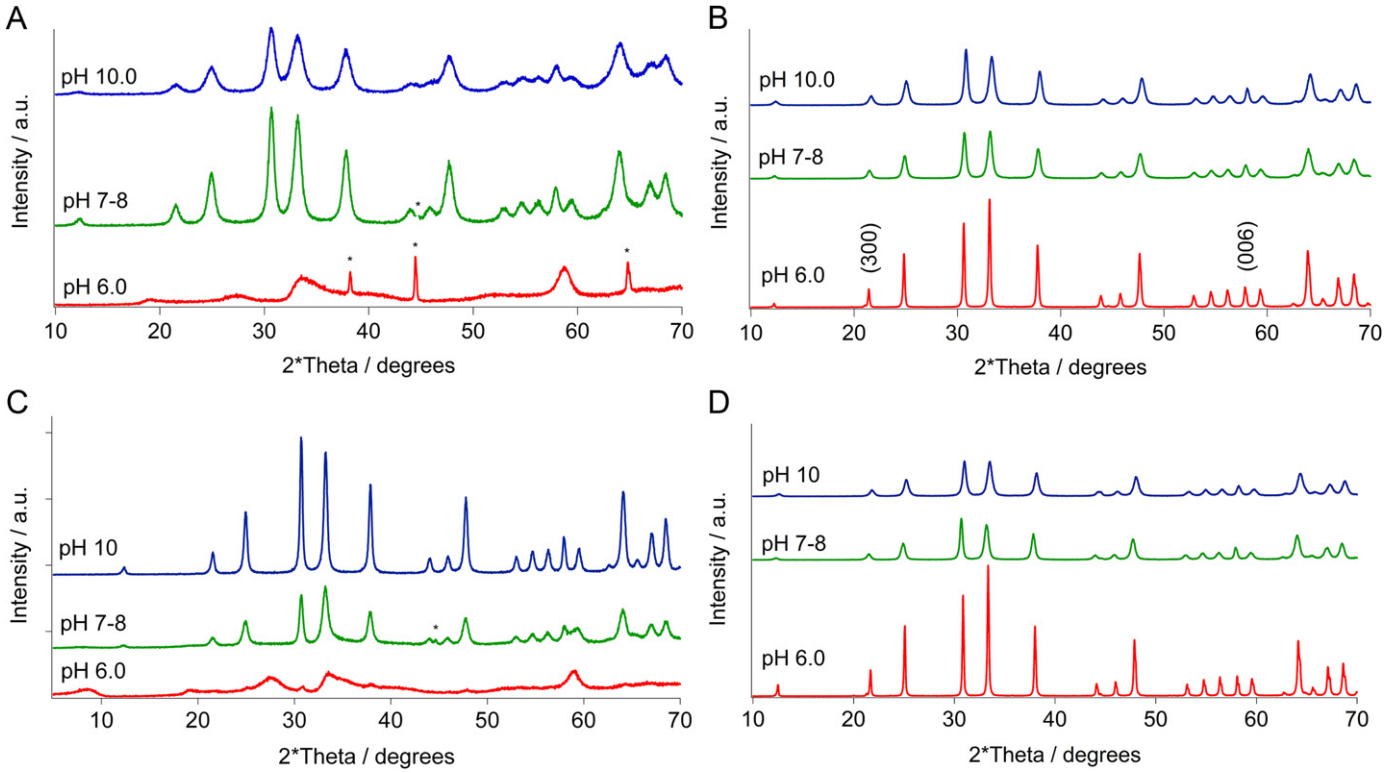

Fig. 1. XRD patterns of Zn_2GeO_4 samples obtained with Zn/Ge=2 (stoic) at 25 °C (A) and at 140 °C (B) and with Zn/Ge=1.25 (excess Ge) at 25 °C (C) and at 140 °C (D) and 8 h synthesis time at various pH conditions. The reflections marked with * correspond to the aluminum in the sample holder. The values in parenthesis are the indexed diffraction planes for the hexagonal cell.

for Zn and negatively by ≈0.4 eV for Ge compared to the standards (ZnO Zn $2p_{3/2}$ is at 1021.4 eV and GeO_2 Ge $2p_{3/2}$ is at 1220.2 eV, Table 3). These shifts in the EBE are due to the movement of some electron density from Zn to the more electronegative Ge (i.e., 1.65 compared to 2.01, respectively). The Zn $2p_{3/2}$ peak position of 1022 eV is close to the value observed by Parhi and Manivannan [26] and Lin et al. [27] for the related compound Zn_2SiO_4 and identical to the peak position attributed to Zn_2GeO_4 in Ge-doped ZnO films [28].

The local atomic structure in the photocatalyst was characterized by Raman spectroscopy (Fig. 4A). We observed a complex band from 700 to 840 cm^{-1} for all the samples prepared at 140 °C. This spectrum is very different from the spectrum of ZnO, but very similar to the Raman spectrum of amorphous GeO_2. By analogy, the Raman bands of zinc germanate are tentatively assigned to the Ge motion (1), Ge–O–Zn symmetric stretch (2), defect oxygen mode (3), Ge–O–Zn bend (4) and Ge–O–Zn asymmetric stretch (5) (see Fig. 4B) [29]. GeO_2 exists in 2 crystalline forms; trigonal, with tetrahedral Ge (space group $P3_221$) and tetragonal with octahedral Ge (rutile form, $P4_2/mnm$) and an additional glassy form which also consists of GeO_4 tetrahedra but lacks uniformity associated with the trigonal crystals [29]. This Raman spectrum of Zn_2GeO_4 is unlike the spectra of the 2 crystalline forms of GeO_2 but interestingly is similar to what was reported for GeO_2 glass [29,30]. Thus, the local structure of Zn_2GeO_4, as determined from Raman analysis, resembles GeO_4 tetrahedra as found in GeO_2 glass rather than as found in crystalline trigonal GeO_2. This suggests that the GeO_4 tetrahedra in zinc germanate are probably vibrationally decoupled from each other. The defect band is assigned to the motion of bridging oxygen atoms from the presence of three-membered GeO_4 rings and suggests the presence of a small fraction of three-membered tetrahedra apart from the usual six-membered GeO_4 tetrahedra.

3.3. Time series synthesis studies

For the same photocatalyst loading (by weight) the materials obtained from solutions prepared at a pH of 7.5 and 10 were the most active for methylene blue degradation (see below). Thus for these 2 catalysts the product was investigated at varying synthesis time from 2 to 24 h to optimize for the rate of dye degradation. All products were stoichiometric zinc germanate independent of the heating time. As was observed for the ET2_8 sample, Zn_2GeO_4 nano-rods were obtained at longer synthesis time (Figs. S4 and S7) and the product surface areas decreased with increased heating time. Narrowing of the (006) peak at ~58° 2θ shows that the crystals grow preferentially along the *c*-direction. This is probably because the (001) crystal plane is energetically less stable than the (100) plane for the zinc germanate crystal [31]. Poly-disperse nano-rods were observed for the ST3 time series samples (Fig. S4). A changing fraction of the globular particles on the surfaces of these poly-disperse nano-rods could be the cause of variability in the surface areas of the products obtained at different times (Table 2).

3.4. Formation of Zn_2GeO_4

A binary-oxide compound like zinc germanate can be crystallized if the pH is high enough to dissolve the germanium source, GeO_2 and stabilize the monomers of germanic acid in solution (for example, samples S1_8 and E1_8) but not so high (i.e., 10) that a zinc rich phase precipitates from solution (for example, sample E3_8) [16,32]. Thus, there is effectively a pH window for crystallization as has been previously observed for d^{10} binary oxide compounds like Zn_2GeO_4 [16] and for Zn_2SnO_4 [17].

Zinc germanate could be formed either by a reaction between $Zn(OH)_2$ and $Ge(OH)_4$ by condensation forming metal-oxygen-metal

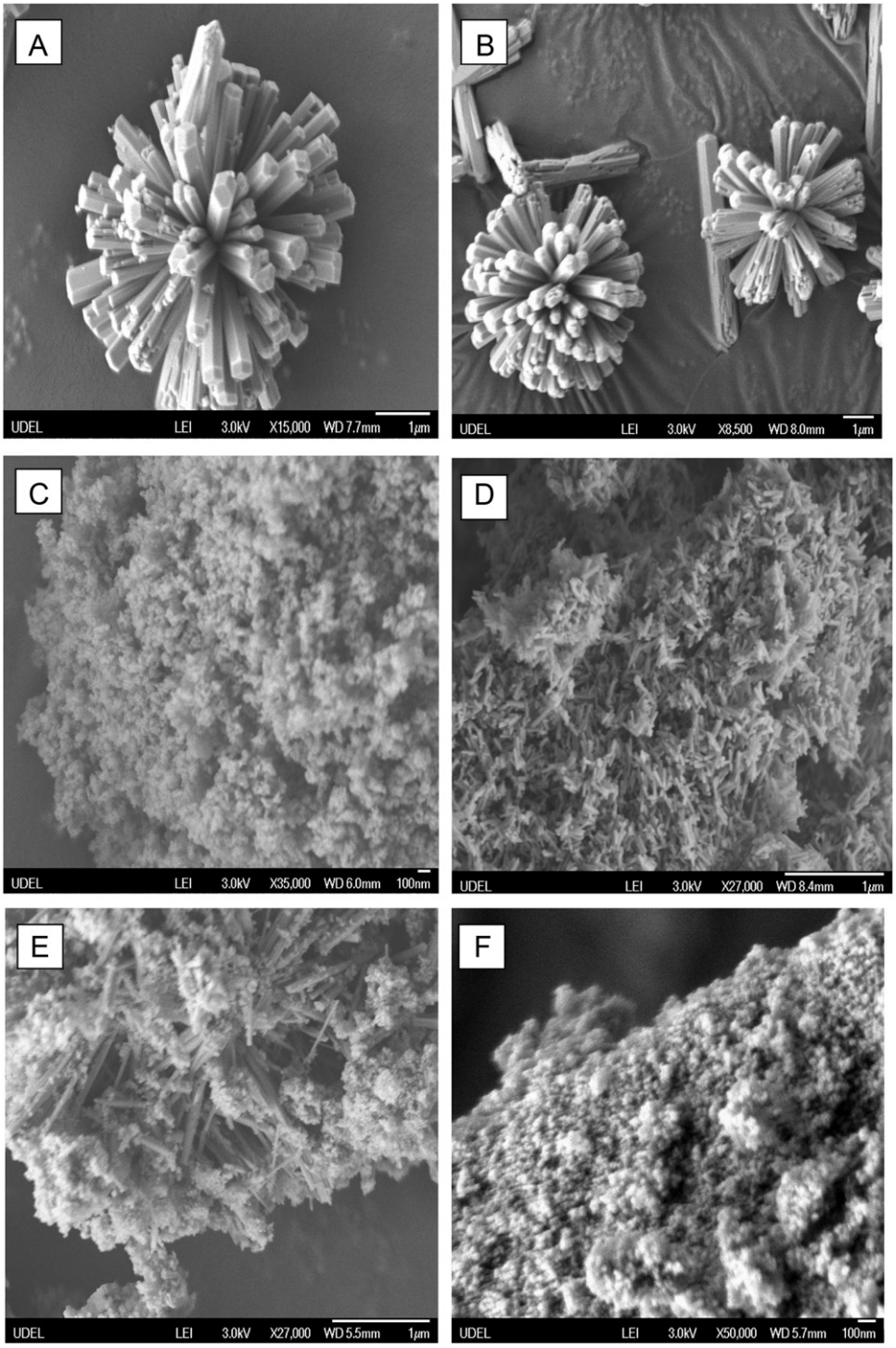

Fig. 2. SEM images corresponding to samples ST1_8 (A), ET1_8 (B), ST2_8 (C), ET2_8 (D), ST3_8 (E) and ET3_8 (F).

bonds (reaction (6)). On the other hand Zn_2GeO_4 could also be formed through an ionic pathway (reactions (7) and (8)).

$$2Zn(OH)_2 + Ge(OH)_4 \rightarrow Zn_2GeO_4 + 4H_2O \quad (6)$$

$$2Zn^{2+} + GeO(OH)_3^- \rightarrow Zn_2GeO_4 + 3H^+ \quad (7)$$

$$2Zn^{2+} + Ge(OH)_4 \rightarrow Zn_2GeO_4 + 4H^+ \quad (8)$$

The initial conductivity of the synthesis gel is determined by Zn^{2+} ions as a result from the dissolution of zinc nitrate hydrate. Addition of GeO_2 has no effect on the conductivity but decreases the pH to ≈ 5.0, a result of the formation and dissociation of germanic acid (pK_a^1 and pK_a^2 for the dissociation of $Ge(OH)_4$ is 9.3 and 12.4, respectively, at 25 °C) [33]. This behavior is similar to the reduction of pH observed during the hydrolysis of tetraethylorthosilicate and tetraethylorthogermanate [25,34]. A Ge rich phase (Fig. 1A) is detected when the synthesis temperature is 25 °C and pH 6 as was also observed in ref [16]. However, when the synthesis temperature is increased to 140 °C, the formation of this additional phase is completely suppressed probably from increased solubility of the additional Ge species.

Table 2
Crystallite sizes determined from the (006) and (300) reflections and specific surface areas (BET) of selected Zn_2GeO_4 photocatalysts (time series experiments).

Sample	Crystallite size along *c*-direction (nm)	Crystallite size along *a*-direction (nm)	Specific surface area ($m^2\,g^{-1}$)
ST2_2	26	16	68
ST2_8	29	20	57
ST2_16	32	23	41
ST2_24	28	23	49
ST3_2	25	15	65
ST3_8	35	18	43
ST3_16	34	18	57
ST3_24	35	20	50
ET2_2	46	22	40
ET2_8	40	21	40
ET2_16	49	28	34
ST2_24	54	33	28
ET3_2	27	15	68
ET3_8	28	18	60
ET3_16	32	18	62
ET3_24	32	18	66

When the pH of the solution is increased from 6.0 to 7.5, the yields are the highest as reaction 6 is not limited either from low concentrations of germanium or zinc hydroxides. It is interesting to note that at the end of the synthesis, a higher pH is observed from the initial 7.5 (Table 1) possibly from the presence of an ammonia buffer. This sets the equilibrium in Eq. (6) to the right; similar to what has been observed for silicic acid in solution [35,36].

When the alkalinity of the solution is higher (pH 10), the pH is constant throughout the synthesis time because it is controlled by the initial surplus amount of hydroxyl anions from the excess ammonia. The yields decrease from the yield observed at pH 7.5 (Table 1). The reductions in the yields at a pH of 10 compared with the maximum yields obtained at pH 7.5 could be from the formation of soluble zinc–ammonia complexes in small concentrations, $[Zn(NH_3)_4]^{2+}$ [37]. These zinc–ammonia complexes though formed, decompose to $Zn(OH)_2$, $Zn(OH)_3^-$ and $Zn(OH)_4^{2-}$at temperatures above 60 °C as detailed by Richardson and Lange [37]. Thus, small concentrations of these zinc complexes could contribute to reductions in the yield observed at pH 10 compared with the yields obtained at pH 7.5 since Zn is the limiting reagent. No increase in the yields was observed with increase in synthesis times (see Section 3.3) suggesting that the yields are limited by the equilibrium solubility of Zn_2GeO_4. The yields are

Table 3
Bulk and surface atomic compositions, binding energies of Ge and Zn representative peaks from XPS.

Sample	EDAX Zn/Ge	XPS Zn/Ge	Ge $2p_{3/2}$ (eV)	Zn $2p_{3/2}$ (ev)
ST1_8	2	2.1	1219.9	1022.0
ST2_8	2	1.9	1219.8	1021.9
ST3_8	2	1.8	1219.8	1021.9
ET1_8	2	2	1219.8	1022.0
ET2_8	2	1.9	1220.1	1022.1
ET3_8	2	1.9	1220.1	1022.1

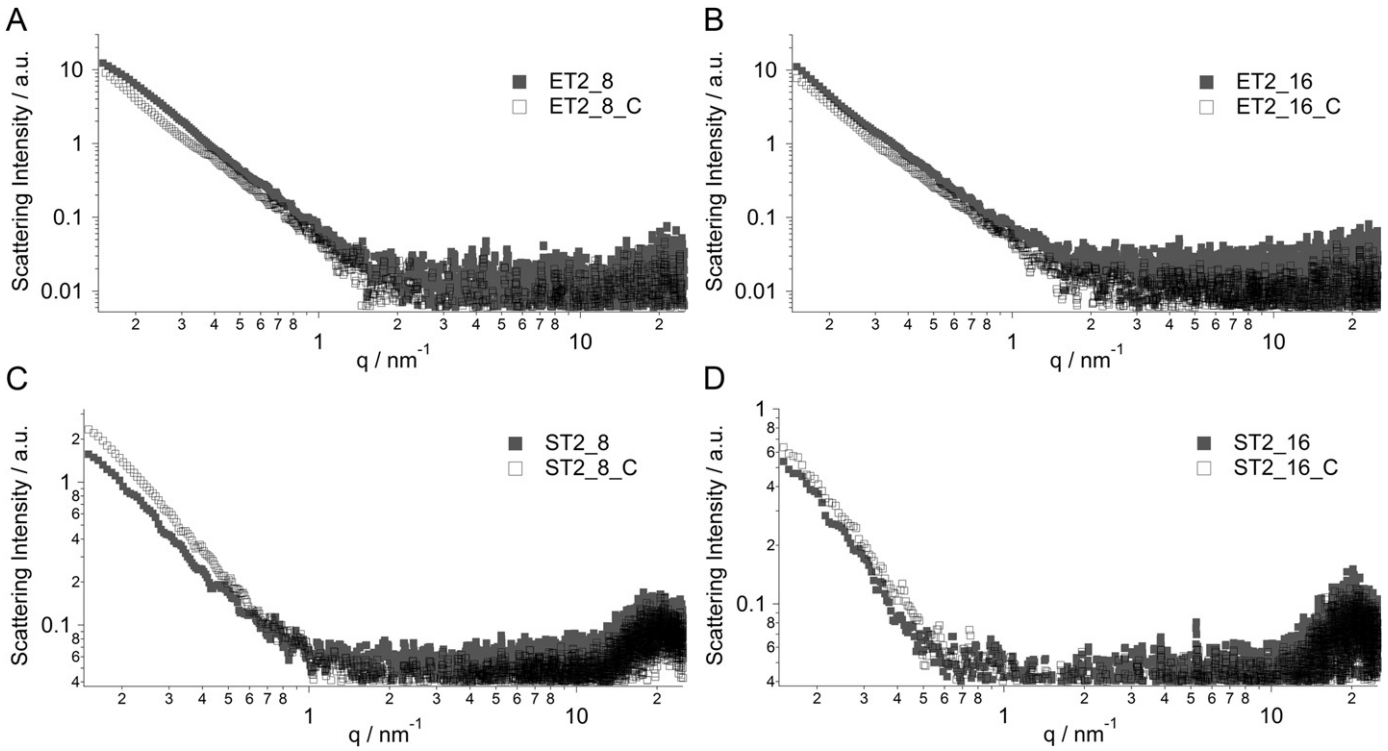

Fig. 3. SAXS measurements of the solutions at the end of the synthesis time with and without CTAB synthesized when initial Zn/Ge ratio is 1.25 (A, B) and the related samples when the initial Zn/Ge ratio is 2 (C, D).

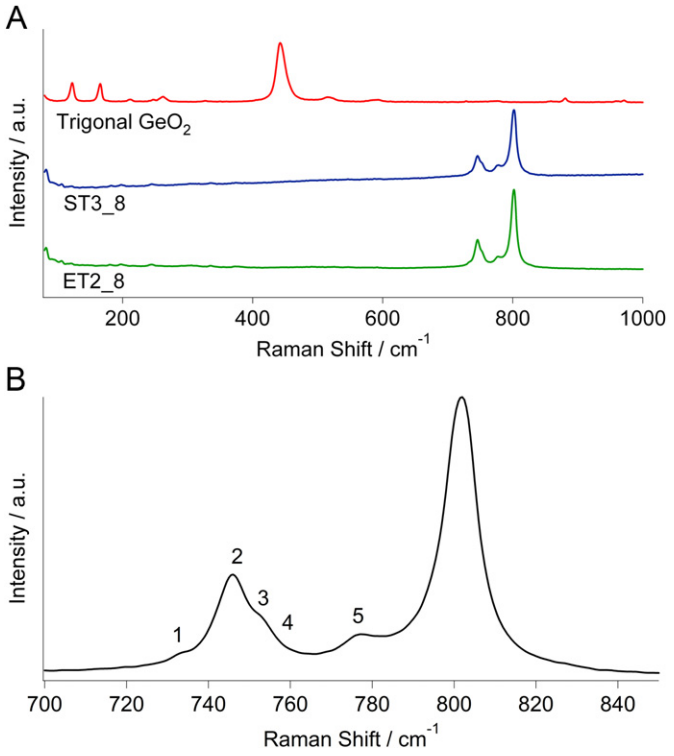

Fig. 4. Raman spectrum (A) of the Zn_2GeO_4 nano-rod photocatalyst. The spectrum of trigonal GeO_2 is provided for reference. The zoomed Raman spectrum from 700 to 840 cm^{-1} of ET2_8 (B) shows the 5 bands tentatively assigned to Ge motion (1), Ge–O–Zn symmetric stretch (2), defect oxygen mode (3), Ge–O–Zn bend (4) and Ge–O–Zn asymmetric stretch (5).

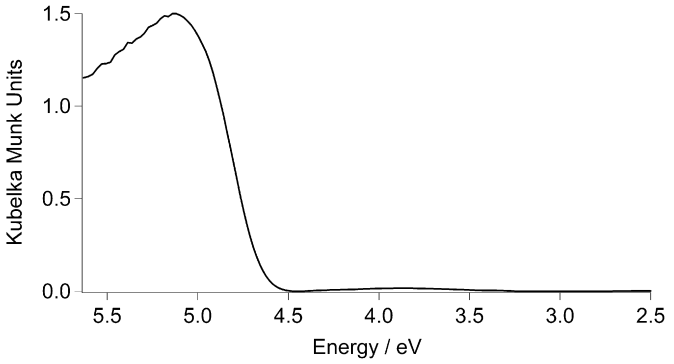

Fig. 5. Diffuse reflectance spectra for the Zn_2GeO_4 nano-rods (ET2_8 sample), the UV–vis spectra for the other zinc germanate samples synthesized at 140 °C are presented in Supporting Information and are similar.

limited by the solubility or lack thereof of appropriate Zn and Ge species, for example, the formation of tetra-ammine zinc complexes reduces the concentration of available Zn^{2+}.

3.5. Photocatalytic activity

The band gap of Zn_2GeO_4 calculated using Davis and Mott's equation [21,38], irrespective of the sample preparation time, pH or CTAB the band gap is ≈4.67 eV (Fig. 5). Methylene blue was used as a model compound for evaluating the photocatalytic activities of the synthesized zinc germanate particles as it is straight forward to follow the degradation rate by UV–vis spectroscopy. A typical degradation curve of methylene blue upon irradiation with ultraviolet light using Zn_2GeO_4 photocatalyst is presented in Fig. 6. The absorbance of methylene blue (at 664 nm) decreases monotonically with illumination time.

Fig. 7a shows the degradation curves of the dye using the samples prepared at 140 °C. The sample synthesized at pH 6.0 was

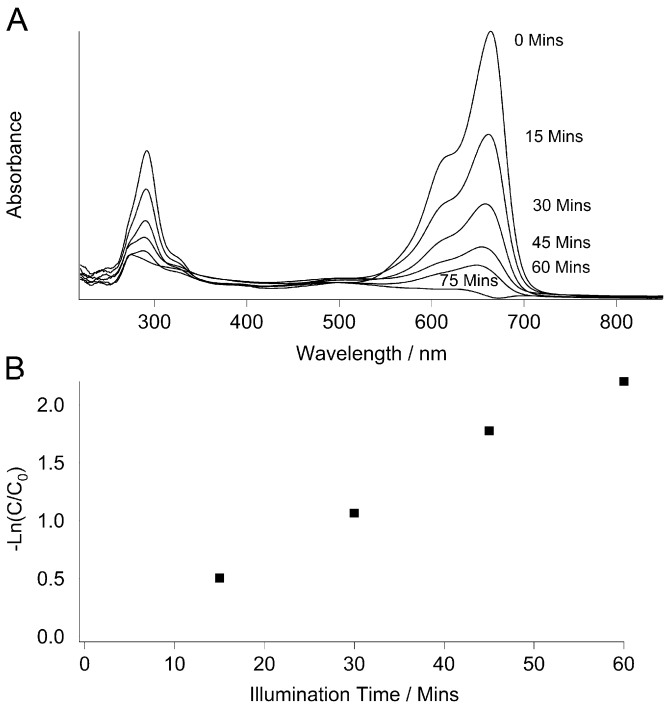

Fig. 6. Representative methylene blue dye degradation temporal profile (A) versus time using Zn_2GeO_4 ET2_8 nano-rods as photocatalyst. 100% conversion was reached within 75 min of illumination time. The points representing the first order rate curve (B) wherein the slope is the effective kinetic constant k (min^{-1}, the catalyst loading is 0.1 g) and the intercept is 0.

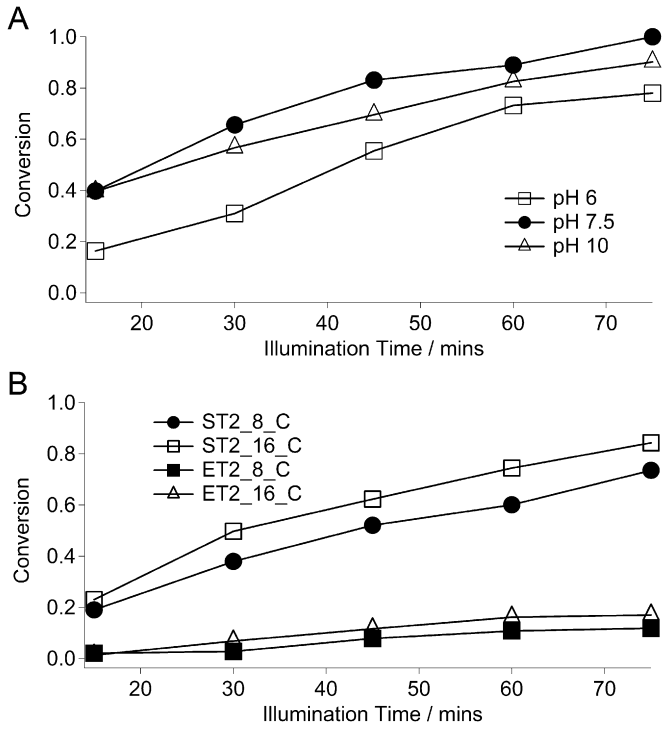

Fig. 7. Methylene blue dye degradation profile using Zn_2GeO_4 photocatalyst synthesized at various pH conditions (samples ET1_8, ET2_8 and ET3_8, A) and using pH 7.5 Zn_2GeO_4 photocatalysts synthesized with CTAB (B).

the least active (for the same catalyst loading of 1 g/l). These large flower-shaped particles however show the highest activity per unit of surface area of catalyst (Table 4). Although the surface areas of the nano-rods (ET2 series) are lower than the corresponding samples with no nano-rods (ST2 and ET3 series, Table 2), the activity of the former is higher (Table 4). This indicates that the nano-rod and flower morphologies favor the diffusion of electrons and holes to the surface thereby increasing the photocatalytic activity. Morphological dependence of electron-hole transport processes has also been observed for photocatalysts with star-like morphologies (with lower surface areas) such as $BiVO_4$ [39].

The time series of the mono-disperse nano-rods (ET2 time series) showed optimal activity for samples heated for 8 h (Table 4). The sample at 8 h has the highest specific surface area among the nano-rod shaped particles (Table 2). No clear trend was observed in the reaction rates when comparing the ET2 nano-rod with ST3 sample sets. It seems that irrespective of the fact that the ST3 samples are poly-morphic, no appreciable decrease in the reaction rates was noticed (Table 4). This is interesting because it has been shown earlier that the increased surface roughness of zinc gallium oxynitrides and bismuth vandates decrease photocatalytic activities [12,40]. The fluctuations in the rates with no specific trend could be because the poly-disperse nano-rods possess higher surface areas.

When CTAB was added to the samples (ST2_8 and ST2_16) a decrease in the activities was observed (Fig. 7B, Table 4). This effect was more pronounced when the CTAB was added to the solutions precipitating the nano-rods (ET2_8_C, ET2_16_C). CTAB (that is, Br_{3d} anions) was observed by XPS indicating that the CTAB is not completely washed out prior to the use of the samples as catalysts. This was corroborated by TGA measurements [41] which show the highest weight loss (Fig. S8) for these samples. This result indicates that CTAB adsorbs on the nano-rod surface [17], hindering methylene blue degradation even though it does not direct the formation of mono-disperse nano-rods.

Table 4
Effective reaction rates and rate constants per gram of catalyst (the catalyst loading is constant at 0.1 g) for methylene blue degradation using various Zn_2GeO_4 photocatalysts. The sample with the highest rate constant (per gram of the catalyst) is in bold.

Sample	Rate constant, k (10^2 min^{-1} g^{-1})	Reaction rate, r_0 (10^2 mg l^{-1} min^{-1} g^{-1})	Half-life $t_{1/2}$ (min)
ST2_2	9.8	49	70.7
ST2_8	26.2	131	26.5
ST2_8_C	16.6	83	41.8
ST2_16	25.8	129	26.9
ST2_16_C	24	120	28.8
ST3_2	23.6	118	29.4
ST3_8	37	185	18.7
ST3_16	20.4	102	34
ST3_24	15.1	75.5	46
ET2_2	22	110	31.5
ET2_8[a]	**37.3**	**186.5**	**18.6**
ET2_8_C	1.7	8.5	408
ET2_16	26.4	132	26.3
ET2_16_C	2.6	13	267
ET2_24	12.5	62.5	55.5
ET3_2	22	110	31.5
ET3_8	29.5	147.5	23.5
ET3_16	20.9	104.5	33.2

[a] The catalyst with the highest rate constant (per surface area) is ET1_8, k is 0.049 min^{-1} m^{-2} compared with k=0.0093 min^{-1} m^{-2} for ET2_8 (Fig. 7A).

4. Conclusions

Hydrothermal synthesis is an effective method to synthesize zinc germanate with good control over the product properties. Novel morphological changes with pH were observed at 140 °C (from flower-shaped at pH 6 to nano-rods at pH 7.5 and then to globular particles at pH 10) when excess germanium was introduced in the reaction solution. The samples at 140 °C were all pure Zn_2GeO_4 with band gaps of $\approx$4.67 eV. Systematic study of the parameters of the hydrothermal synthesis protocol provided insight into the factors affecting the crystal growth from solution. Temperature, pH and germanium in solution, rather than CTAB, were found to be effective in the synthesis of nano-rods. Adsorbed CTAB was also shown to decrease the photocatalytic activities. The large flower shaped particles show the highest activity per surface area whereas the nano-rods were the most effective in dye degradation per unit mass of catalyst. Among the nano-rods, the highest activity was obtained when the heating time was 8 h corresponding to the formation of mono-disperse nano-rod shaped particles with the highest surface area among the ET2 sample set.

Supporting information available

XRD patterns, UV–vis spectra and SEM micrographs of the associated compounds, TGA data corresponding to the CTAB samples, further analysis on the samples synthesized at 25 °C. This material is available free of charge via the Internet.

Acknowledgments

The authors would like to acknowledge N. Menagazzo for help with the measurement of the Raman scans, A. Foster for help with the TGA scans, C. Weiland for training with the XPS equipment and C. Ni and F. Kriss (of the W. M. Keck Electron Microscopy Facility at the University of Delaware) for providing the SEM time and help. Funding for this research was provided by the U.S. Department of Energy Basic Energy Sciences under Grant nos. DE-FG02-07ER15921 and DE-FG02-99ER14998. We thank the reviewers for their valuable suggestions.

Appendix A. Supporting materials

Supplementary data associated with this article can be found in the online version at doi:10.1016/j.jssc.2011.02.022.

References

[1] A.L. Linsebigler, G. Lu, J.T. Yates, Chem. Rev. 95 (1995) 735.
[2] G. Liu, L. Wang, H.G. Yang, H.-M. Cheng, G.Q. Lu, J. Mater. Chem. 20 (2009) 831.
[3] Y. Inoue, Energy Environ. Sci. 2 (2009) 364.
[4] K. Maeda, K. Domen, Chem. Mater. 22 (2009) 612.
[5] K. Ikarashi, J. Sato, H. Kobayashi, N. Saito, H. Nishiyama, Y. Inoue, J. Phys. Chem. B 106 (2002) 9048.
[6] A. Kudo, Y. Miseki, Chem. Soc. Rev. 38 (2009) 253.
[7] F.E. Osterloh, Chem. Mater. 20 (2007) 35.
[8] C. Hang, M.A. Simonov, N.V. Belov, Sov. Phys. Crystallogr. USSR 15 (1970) 387.
[9] C.-C. Hung, M.-P. Chang, C.-Y. Ho, C.-K. Yu, W.-T. Lin, J. Electrochem. Soc. 157 (2010) K80.
[10] Z.N. Wang, M.F. Jiang, J.Y. Ning, L. Zhu, Acta Phys. Sin. 57 (2008) 6507.
[11] J. Sato, H. Kobayashi, K. Ikarashi, N. Saito, H. Nishiyama, Y. Inoue, J. Phys. Chem. B 108 (2004) 4369.
[12] J. Yu, A. Kudo, Adv. Funct. Mater. 16 (2006) 2163.
[13] B.B. Kale, J.O. Baeg, S.M. Lee, H. Chang, S.J. Moon, C.W. Lee, Adv. Funct. Mater. 16 (2006) 1349.

[14] S. Shuyan, Z. Yu, X. Yan, W. Cheng, F. Jing, S. Weidong, Z. Guoli, Z. Hongjie, Adv. Funct. Mater. 18 (2008) 2328.
[15] Z. Lisha, W. Wenzhong, Z. Lin, X. Haolan, Small 3 (2007) 1618.
[16] H. Jianhui, D. Kaining, H. Yidong, W. Xinchen, F. Xianzhi, ChemSusChem 1 (2008) 1011.
[17] J. Zeng, M. Xin, Li, H. Wang, H. Yan, W. Zhang, J. Phys. Chem. C 112 (2008) 4159.
[18] B. Ma, F. Wen, H. Jiang, J. Yang, P. Ying, C. Li, Catal. Lett. 134 (2010) 78.
[19] J. Huang, X. Wang, Y. Hou, X. Chen, L. Wu, X. Fu, Environ. Sci. Technol. 42 (2008) 7387.
[20] Q. Liu, Y. Zhou, J. Kou, X. Chen, Z. Tian, J. Gao, S. Yan, Z. Zou, J. Am. Chem. Soc. 132 (2010) 14385.
[21] E.A. Davis, N.F. Mott, Philos. Mag. 22 (1970) 903.
[22] A. Houas, H. Lachheb, M. Ksibi, E. Elaloui, C. Guillard, J.-M. Herrmann, Appl. Catal. B 31 (2001) 145.
[23] M.R. Hoffmann, S.T. Martin, W. Choi, D.W. Bahnemann, Chem. Rev. 95 (1995) 69.
[24] M.-Y. Tsai, C.-Y. Yu, C.-C. Wang, T.-P. Perng, Cryst. Growth Des. 8 (2008) 2264.
[25] T.M. Davis, M.A. Snyder, M. Tsapatsis, Langmuir 23 (2007) 12469.
[26] P. Parhi, V. Manivannan, J. Alloys Compd. 469 (2009) 558.
[27] C.M. Lin, Y.Z. Tsai, J.S. Chen, Thin Solid Films 515 (2007) 7994.
[28] M. Jiang, Z. Wang, Z. Ning, Thin Solid Films 517 (2009) 6717.
[29] M. Micoulaut, et al., J. Phys.: Condens. Matter 18 (2006) R753.
[30] G.S. Henderson, D.R. Neuville, B. Cochain, L. Cormier, J. Non-Cryst. Solids 355 (2009) 468.
[31] C. Sun, C. Kuan, F.J. Kao, Y.M. Wang, J.C. Chen, C.C. Chang, P. Shen, Mater. Sci. Eng.: A 379 (2004) 327.
[32] J.-M. Jang, S.-D. Kim, H.-M. Choi, J.-Y. Kim, W.-G. Jung, Mater. Chem. Phys. 113 (2009) 389.
[33] J.D. Rimer, D.D. Roth, D.G. Vlachos, R.F. Lobo, Langmuir 23 (2007) 2784.
[34] T. Kawai, Y. Usui, K. Kon-No, Colloids Surf. A: Physicochem. Eng. Aspects 149 (1999) 39.
[35] S. Yang, A. Navrotsky, Chem. Mater. 14 (2002) 2803.
[36] N.D. Hould, R.F. Lobo, Chem. Mater. 20 (2008) 5807.
[37] J.J. Richardson, F.F. Lange, Cryst. Growth Des. 9 (2009) 2570.
[38] M.J. Nash, S. Rykov, R.F. Lobo, D.J. Doren, I. Wachs, J. Phys. Chem. C 111 (2007) 7029.
[39] S. Sun, W. Wang, L. Zhou, H. Xu, Ind. Eng. Chem. Res. 48 (2009) 1735.
[40] H. Takashi, M. Kazuhiko, L. Daling, D. Kazunari, ChemSusChem 2 (2009) 336.
[41] A.-C. Lee, R.-H. Lin, C.-Y. Yang, M.-H. Lin, W.-Y. Wang, Mater. Chem. Phys. 109 (2008) 275.